

Cite this: *J. Mater. Chem. C*, 2017,
5, 7084

Enhanced physical properties of pulsed laser deposited NiO films *via* annealing and lithium doping for improving perovskite solar cell efficiency†

Zhiwen Qiu,^{ab} Haibo Gong,^a Guanhaojie Zheng,^b Shuai Yuan,^a Hailiang Zhang,^a
Xiaomeng Zhu,^a Huanping Zhou ^{*b} and Bingqiang Cao ^{*ac}

Pulsed laser deposition (PLD) is a powerful growth technique for thin films, where *in situ* doping and post-thermal annealing are the most effective ways to tune the crystalline and physical properties of the deposited films. This paper demonstrates that the crystallinity, transparency, and electrical properties of NiO films are well controlled by PLD, which determines the photovoltaic performance of CH₃NH₃PbI_{3-x}Cl_x-based perovskite solar cells with NiO films as the hole transport layers (HTLs). After post-annealing, the NiO films exhibit enhanced in-plane crystal orientation, high transmittance, and uniform surface morphology, and, accordingly, the power conversion efficiency (PCE) of the perovskite solar cell improves from 5.38% to 12.59%. Moreover, by doping the ablated target with lithium (Li), PLD can produce doped NiO:Li films with significantly enhanced electrical conductivity, which further improves the perovskite cell PCE from 12.59% to 15.51%. These results highlight the importance of optimizing the transporting layer properties toward high-performance inverted perovskite planar solar cells.

Received 23rd March 2017,
Accepted 28th June 2017

DOI: 10.1039/c7tc01224a

rsc.li/materials-c

1. Introduction

Since the organometal halide perovskite (CH₃NH₃PbX₃, X: Cl, Br, or I) sensitized solar cells were firstly reported by Miyasaka *et al.*,¹ a major scientific breakthrough in the field of photovoltaics has been the emergence of organometal perovskites as light absorber materials, achieving exceptional progress in photovoltaic efficiency improvement.² Typically, CH₃NH₃PbI₃ (MAPbI₃) has a direct optical band gap of around 1.5 eV,³ low exciton binding energy (2–55 meV),^{4–7} and apparent tolerance of structural defects. Another superior property of such perovskites for solar cell applications is the high optical absorption coefficient (~10⁴ cm⁻¹). An absorber layer less than 500 nm thick can absorb sunlight (<780 nm) effectively to achieve a high efficiency. More recently, it has been observed that perovskite materials exhibit long charge carrier diffusion lengths (for CH₃NH₃PbI_{3-x}Cl_x film >1 μm) and thus can be used for planar film solar cells.⁸ So far, the most efficient planar perovskite solar cells with PCEs over 15%

have a typical layered P–i–N (or N–i–P) film structure of HTL/perovskite/ETL (or ETL/perovskite/HTL), where HTL and ETL represent the p-type (P) hole transport layer and n-type (N) electron transport layer, respectively, and intrinsic (i) perovskite as an active layer.^{9–11} The ETL and HTL layers not only collect the currents but block the holes and electrons, respectively. They also prevent the perovskite active layer from directly contacting the electrodes to reduce recombination of photocarriers.¹² Taking the inverted P–i–N solar cell as an example, the film roughness of the HTL also influences the following growth of the perovskite layer, especially for the interface between the HTL and the perovskite. Moreover, the electrical and optical properties of the HTL can significantly influence the performance of perovskite solar cells (PSCs) in terms of fill factor (FF), open-circuit voltage (V_{oc}), and short-circuit current (J_{sc}). So, selecting a HTL with controlled physical properties is essential to understand the device photovoltaic processes such as carrier separation, transport, extraction, and recombination.^{13,14}

At present, semiconducting polymers like Spiro-OMeTAD and PEDOT:PSS are widely used as HTLs. However, Spiro-OMeTAD is relatively expensive and needs p-type doping for optimal cell performance,¹⁵ and PEDOT:PSS is also not an ideal HTL material because of its inefficient electron-blocking capability and poor chemical stability due to its hygroscopic nature.^{16–18}

Compared to organic HTLs, inorganic HTLs have several advantages like low cost, environmentally friendliness, good stability,

^a Materials Research Center for Energy and Photoelectrochemical Conversion, School of Material Science and Engineering, University of Jinan, Jinan 250022, Shandong, China. E-mail: mse_caobq@ujn.edu.cn

^b Department of Materials Science and Engineering, College of Engineering, Peking University, Beijing 100871, China. E-mail: happy_zhou@pku.edu.cn

^c Department of Physics and Institute of Laser, Qufu Normal University, Qufu, 273165, China

† Electronic supplementary information (ESI) available. See DOI: 10.1039/c7tc01224a

and high hole mobility. As a cubic p-type semiconductor with a suitable band gap, an inorganic NiO film can act as a stable HTL for perovskite solar cells due to its inherent material properties.¹⁹ Moreover, the high work function (~ 5.0 eV) affords the promise of higher device open-circuit voltage.²⁰ Jeng *et al.*²¹ first reported a MAPbI₃ based solar cell using a NiO_x thin layer as the HTL with a PCE of 7.8%. Subsequently, Wang *et al.*²² applied a mesoscopic (mp) NiO film on the top of a NiO_x layer as a composite HTL. However, only a relatively low J_{sc} of 13.24 mA cm⁻² and a fill factor (FF) of 0.69 were achieved. Recently, they improved the overall device efficiency to 11.6% by sputtering the NiO_x films instead of using a solution process.²⁰ But, the relatively thick mp-NiO layer exhibits severe light absorption and results in a low external quantum efficiency (EQE) that is less than 70% below 500 nm. Moreover, stoichiometric NiO is an insulator with a resistivity as high as 10¹³ Ω cm at room temperature.²³ The electrical properties of NiO thin films are primarily determined by the holes generated from nickel vacancies, interstitial oxygen atoms, and intentional dopants. The resistivity of NiO films can be decreased by doping with monovalent impurities including copper (Cu) and lithium (Li).^{24–26} Another problem is that, although it is low-cost, lower-temperature solution processing generally produces oxide thin films with defects and uncontrolled dopants/impurities, which can cause degradation for light transmission and carrier transport properties.²⁷ Therefore, it is of clear significance to regulate the physical properties of NiO such as transparency and conductivity for HTL applications in perovskite solar cells. But the current progress is not smooth and there is a dearth of effort in this area.

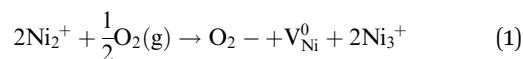
The pulsed laser deposition (PLD) growth technique can grow oxide films with less impurities and better crystallinity and has several advantages to adjust their physical properties by controlling the experimental conditions and *in situ* doping growth. In this paper, we studied systematically the effect of post-annealing and doping growth on the microstructure and semiconducting properties of NiO thin films grown by PLD. As a typical inorganic HTL, its influence on the device performance has been investigated by constructing a planar PSC with NiO/CH₃NH₃PbI_{3-x}Cl_x/PCBM/Ag configuration. With the optimized PLD growth conditions for NiO, a stable and reproducible solar cell efficiency of 5.38–12.59% was obtained. Moreover, doping NiO with lithium (Li) further improved the performance of the cell devices from 12.59% to 15.51%. This study not only revealed the importance of growth optimization for more effective inorganic charge-transporting NiO HTLs, but also provided an excellent device platform by doping NiO layers for making high-performance perovskite solar cells.

2. Results and discussion

2.1 Effect of post-annealing on NiO microstructure and semiconducting properties

Post-annealing has a significant effect on the microstructural properties of NiO films, and further influences the performance of perovskite solar cells. The SEM images of NiO films annealed

at 100–450 °C show a systematic evolution of the surface morphology in Fig. 1(a–f). The surface of the as-prepared NiO film appears relatively rough with nanoparticles, as shown in Fig. 1(a). With the increase of annealing temperature in Fig. 1(b–f), the film surface roughness reduces. When the annealing temperature is up to 450 °C, the film surface is more smooth and dense and the film crystallization quality becomes better. For inverted planar perovskite solar cells, the film roughness of the HTL influences the growth of the perovskite layer, especially for the interface between the HTL/perovskite.²⁸ Fig. 1(g) presents the XRD patterns of the NiO films as a function of annealing temperature. The samples are intentionally grown with a controlled thickness of 100 nm for XRD intensity comparison. The peak at $2\theta \approx 42.6^\circ$ is assigned to the cubic (200) crystalline planes of NiO.³⁰ At a low annealing temperature (100–300 °C), only very weak (200) peaks are found owing to their low film crystallinity. As the annealing temperature increases to 450 °C, the (200)-peak intensity increases indicating that the NiO layer after post-annealing shows better crystallinity. After higher temperature annealing, *e.g.* 400–450 °C, the (200) peaks of the NiO samples obviously shift to higher angles as compared with those of NiO films at 100–300 °C annealing. According to the Bragg formula for XRD, this indicates that the lattice constant shrinks. This is due to the internal lattice stress releasing after the annealing process.³¹ Furthermore, the X-ray photoelectron spectra (XPS) of the as-prepared and annealed at 450 °C NiO films are shown in Fig. S2 (ESI†), respectively. The detailed composition analysis of the Ni 2p and O 1s peaks is shown in Tables S1–S3 (ESI†). It should be mentioned that increasing the annealing temperature does not change the composition of the NiO films significantly. However, the amount of Ni³⁺ [marked as peak (2) in Fig. S2(c and d), ESI†] increases from 22.44% to 26.11%. It is well-known that nickel oxide is a metal deficient p-type semiconductor. Defects are easily formed in an oxygen-rich atmosphere according to the following equation



As shown in eqn (1), the Ni³⁺ is produced by Ni²⁺ to maintain electrical neutrality in the crystal. As a result, the number of Ni³⁺ ions gradually increases after annealing. V_{Ni}⁰ stands for a Ni vacancy, which could further form singly (V'_{Ni}) or doubly (V''_{Ni}) ionized defects associated with hole generation as shown in eqn (2) and (3). V''_{Ni} is the most stable defect within the band gap due to its lower formation energy and one of the most important defects that affect the electrical behavior of the NiO film.³² The XPS analysis can support well the square resistance data shown in Table S7 (ESI†). Fig. 1(h) shows the optical transmittance spectra of the NiO films at different annealing temperatures. The 30 nm thick NiO layer annealed at 450 °C exhibits above 95% transmission over a broad spectral range from 450 to 800 nm using bare ITO glass as the reference. The transmittance values gradually increase with increase in annealing temperature

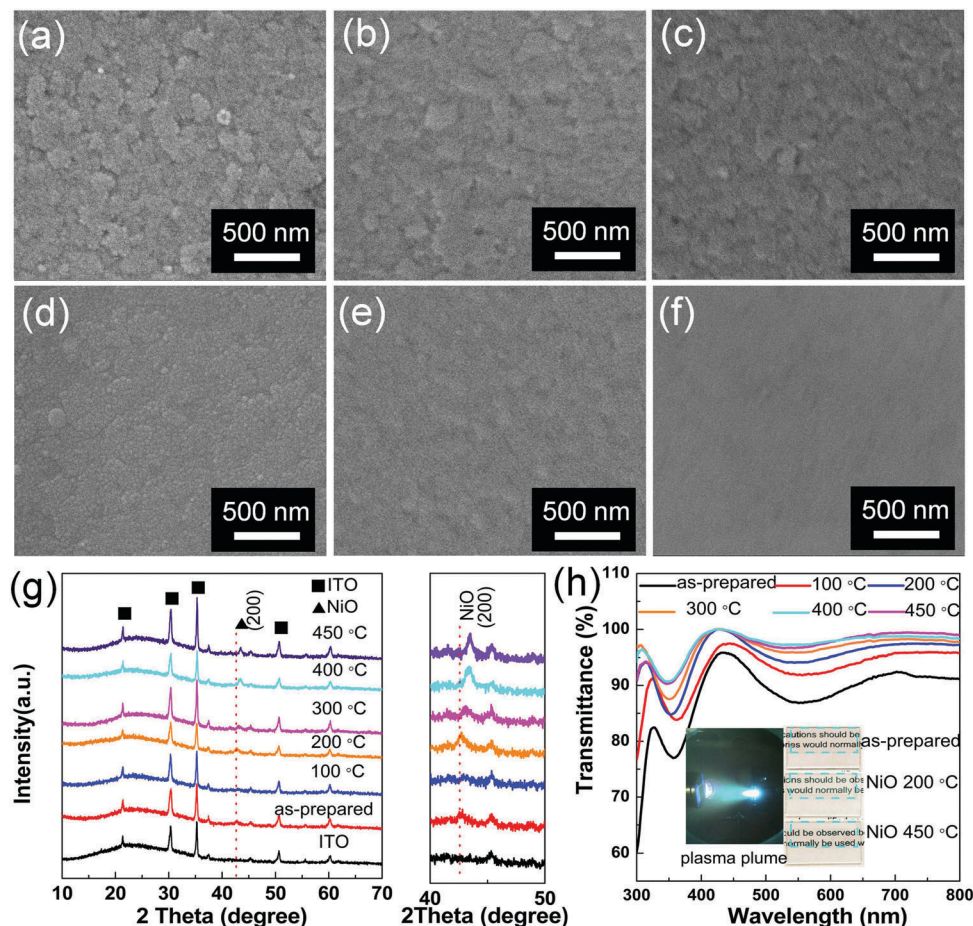


Fig. 1 SEM images showing the general morphology of NiO films with different annealing temperatures (a–f). (a) As-prepared; (b) 100 °C; (c) 200 °C; (d) 300 °C; (e) 400 °C; (f) 450 °C; (g) full-range of XRD patterns taken from NiO films with different annealing temperatures; (h) the transmittance spectra of NiO films prepared at different annealing temperatures (100–450 °C). Inset is the plasma plume and photos of NiO films. The NiO films with different annealing temperatures (as-prepared, 200 °C, 450 °C) on top of the glass/ITO (corresponding to the blue rectangle square part of the inset in (h)) appear transparent, as compared to the patterned ITO substrates.

as the film morphology becomes denser. The high transparency can allow large solar photon flux to reach the $\text{CH}_3\text{NH}_3\text{PbI}_{3-x}\text{Cl}_x$ layer below for photocurrent generation.

Fig. 2(a and b) show the device structure of ITO/NiO/ $\text{CH}_3\text{NH}_3\text{PbI}_{3-x}\text{Cl}_x$ /PCBM/Ag and a typical cross-sectional SEM image of the device, where each layer is marked with a different color. Fig. 2(c) shows the band alignments of the solar cell. The data for the NiO films annealed at different temperatures are taken from the UPS spectra, shown in Fig. S1 (ESI[†]). And the data for $\text{MAPbI}_{3-x}\text{Cl}_x$ and PCBM are taken from ref. 26. When the annealing temperature increases from R.T. to 450 °C, the valence band maximum (E_{VB}) varies from -5.04 eV to -5.25 eV, as shown in Fig. S1 (ESI[†]). The edge level of the valence band (E_{VB} , -5.25 eV) for the NiO film annealed at 450 °C exhibits better alignments with $\text{MAPbI}_{3-x}\text{Cl}_x$ E_{VB} (about -5.43 eV) (refer to Fig. S1 in the ESI[†]). Accordingly, it is anticipated that only a small energy loss will occur, which would facilitate the hole extraction from the perovskite absorber material to the NiO hole transport layer effectively.²⁹ Moreover, such a NiO layer can also efficiently prevent electron leakage due to the sufficiently

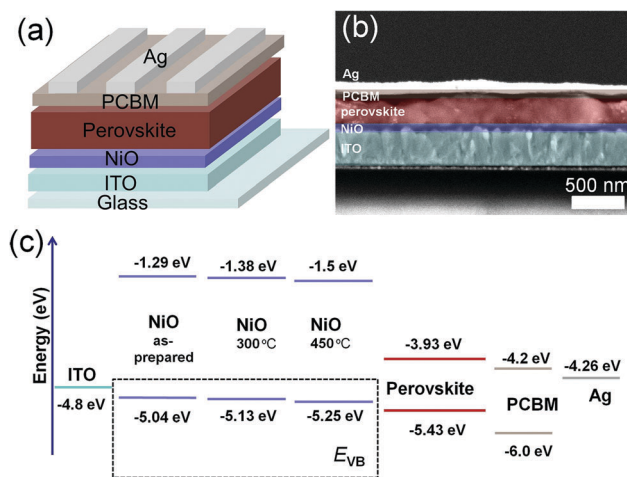


Fig. 2 ITO/PLD-NiO/ $\text{CH}_3\text{NH}_3\text{PbI}_{3-x}\text{Cl}_x$ /PCBM/Ag solar cells. (a) Diagram of the device configuration; (b) cross-sectional SEM image showing the complete device structure; (c) band alignments of the perovskite solar cell.

high conduction band offset between NiO (450 °C, -1.5 eV) and $\text{CH}_3\text{NH}_3\text{PbI}_{3-x}\text{Cl}_x$ (-3.93 eV).²² Similarly, photoelectrons can flow to the Ag contact through the PCBM layer. Therefore, this configuration is suitable for efficient hole–electron dissociation and charge transport.

In order to determine whether NiO films prepared at different annealing temperatures are compatible to act as HTLs for perovskite solar cells, we estimate the NiO quenching ability by measuring the photoluminescence spectra of $\text{CH}_3\text{NH}_3\text{PbI}_{3-x}\text{Cl}_x$ films, as it has become routine in all organic solar cells.³³ Successful charge transfer from $\text{CH}_3\text{NH}_3\text{PbI}_{3-x}\text{Cl}_x$ to NiO is a prerequisite to make efficient solar cells. For a $\text{CH}_3\text{NH}_3\text{PbI}_{3-x}\text{Cl}_x$ film deposited onto a glass substrate, a strong PL peak is observed located at around 767 nm (Fig. 3(a)) with the calculated optical band gap of about 1.61 eV, similar to literature results.³⁴ However, when an additional NiO film is grown on the ITO-glass substrate, the PL from the $\text{CH}_3\text{NH}_3\text{PbI}_{3-x}\text{Cl}_x$ film deposited with an identical process is quenched. Clearly, free holes (or excitons) generated in the $\text{CH}_3\text{NH}_3\text{PbI}_{3-x}\text{Cl}_x$ upon illumination are extracted (or dissociated) by the underlying NiO film, quenching the band edge photoluminescence. The sample with the as-prepared NiO

film exhibits poor quenching rate among all the NiO film samples, as shown in Fig. 3(a). With the increase of annealing temperature, the NiO film quenches the perovskite PL more efficiently. Here the different quenching ability indirectly gives a measure of charge collection efficiency for the NiO layer. The samples with NiO layers annealed at 400 °C and 450 °C exhibit the best quenching efficiency, which indicates that the NiO films annealed at this temperature range are indeed good hole-collecting layers for perovskite solar cells.

To further investigate the perovskite grown on the NiO film, the optical absorption spectra of the PbI_2 films before and after converting to perovskite film are recorded in Fig. 3(b). The absorption spectra of the NiO and PbI_2 films exhibit absorption edges at about 350 and 520 nm, respectively, which both correspond to the band gap absorption as reported.^{35,36} The optical absorption onset of the $\text{CH}_3\text{NH}_3\text{PbI}_{3-x}\text{Cl}_x$ perovskite film occurs at about 770 nm,^{37,38} which is consistent with the PL data.³⁹ Raman spectroscopy is used to further characterize the crystalline structure of NiO, PbI_2 , and $\text{CH}_3\text{NH}_3\text{PbI}_{3-x}\text{Cl}_x$ films, which were excited by a 532 nm laser (3 mW). Fig. 3(c) shows the Raman spectra of the NiO films after annealing, where a transverse optical mode (TOM, 491 cm^{-1}) from the NiO film and two peaks assigned

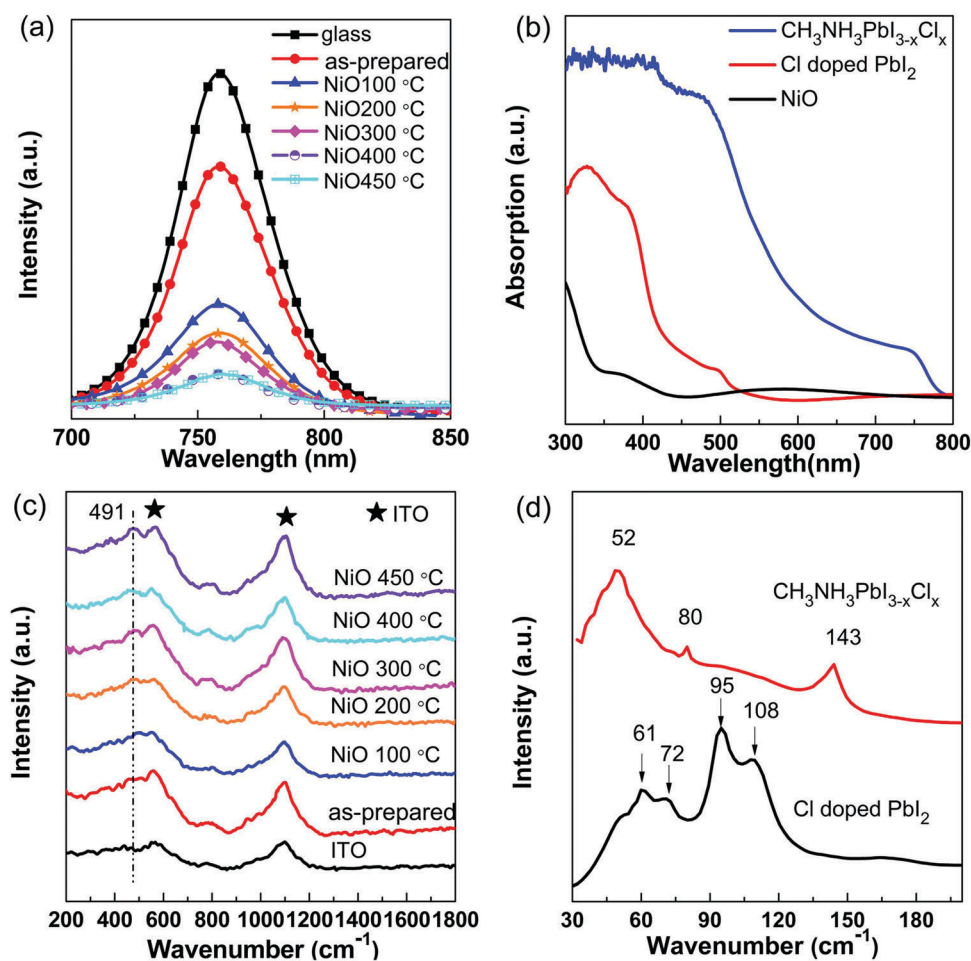


Fig. 3 (a) Steady-state photoluminescence spectra of $\text{CH}_3\text{NH}_3\text{PbI}_{3-x}\text{Cl}_x$ perovskite films coated with NiO films at different annealing temperatures; (b) UV-vis absorption spectra of NiO, Cl doped PbI_2 , and $\text{CH}_3\text{NH}_3\text{PbI}_{3-x}\text{Cl}_x$ films; (c) Raman scattering spectra of NiO films at different annealing temperatures under the excitation source of 532 nm; (d) Raman scattering spectra of a Cl doped PbI_2 film and $\text{CH}_3\text{NH}_3\text{PbI}_{3-x}\text{Cl}_x$ film.

to ITO are observed.⁴⁰ With the increase in annealing temperature, the peak located at 491 cm^{-1} becomes obvious, which further indicates that the crystal quality of the NiO film becomes better. This phenomenon is consistent with the results of XRD (Fig. 1g). The Raman spectra are also measured for PbI_2 and mixed-halide perovskite $\text{CH}_3\text{NH}_3\text{PbI}_{3-x}\text{Cl}_x$ films as shown in Fig. 3(d). Four bands at 61 , 72 , 95 , and 108 cm^{-1} of PbI_2 are observed in the $30\text{--}200\text{ cm}^{-1}$ region, which are the bending mode of the Pb–I bond, the shearing mode of two iodide layers, the symmetric stretching A_{1g} mode of the Pb–I bond, and the longitudinal polar mode E_u^1 of the PbI_2 crystal, respectively.^{39–43} For the mixed-halide perovskite sample, three bands are mainly observed. The bands at 52 and 80 cm^{-1} are mainly associated to the Pb–I bending and stretching modes of MAPbI_3 .⁴⁰ The 143 cm^{-1} band is the libration of the MA cations, which is theoretically calculated at 141 cm^{-1} .⁴⁴

2.2 Effect of post-annealing on the NiO film based PSC performance

To investigate the annealing influence of NiO films on the device photovoltaic performance, the J – V characteristics of the

PLD-NiO/ $\text{CH}_3\text{NH}_3\text{PbI}_{3-x}\text{Cl}_x$ /PCBM heterojunction cells are measured, which are shown in Fig. 4(a). Perovskite $\text{CH}_3\text{NH}_3\text{PbI}_{3-x}\text{Cl}_x$ films were prepared with the two-step sequential deposition method^{28,45,46} as schematically shown in Fig. S3 and S4 (ESI†). The optimized atmosphere and pressure of the PLD-NiO HTL in the device are pure O_2 atmosphere, and 1.33 Pa (see Fig. S5 and S6 and Tables S4 and S5, ESI†). For the thin NiO film, the optimum thickness is found to be 20 nm with the adjusted deposition time (see Fig. S7 and Table S6, ESI†). It should be noted that the J – V test is conducted under ambient atmosphere with a relative humidity (RH) of about 25% and all devices are measured directly without encapsulation. The device performance parameters are summarized in Table 1. When the as-prepared NiO film is incorporated, the device exhibits a J_{sc} of 11.39 mA cm^{-2} , a V_{oc} of 0.96 V , and a PCE of 5.38%. When the annealing temperature increases from 100 to $450\text{ }^\circ\text{C}$, the PCE increases from 7.91% to 12.59% mainly due to the increase in J_{sc} from 14.14 to 19.86 mA cm^{-2} , and FF from 48.6% to 62.78%. Fig. 4(b) shows the corresponding EQE spectra from 300 to 1000 nm . The characteristic absorption edges of all devices appear at 800 nm ,

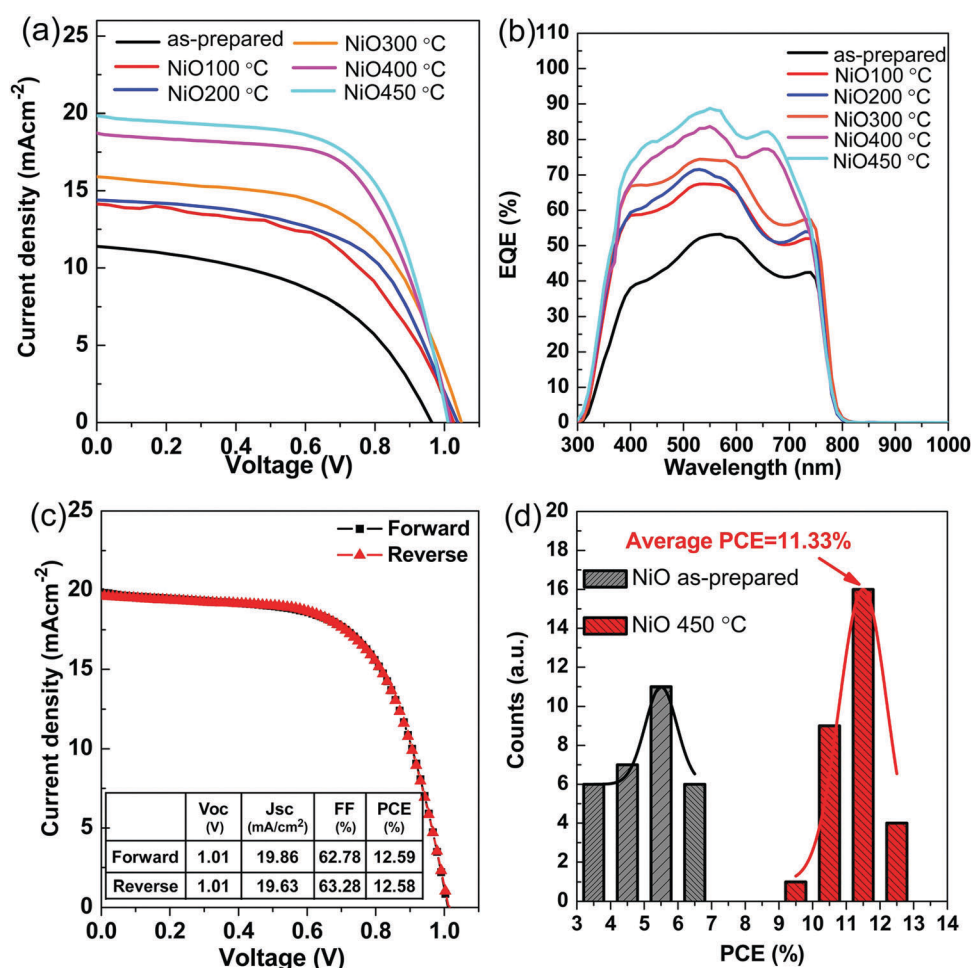


Fig. 4 (a) The photocurrent density–voltage (J – V) curves of perovskite solar cells based on PLD-NiO films with different annealing temperatures (100–450 °C), all of the J – V measurements are carried out under ambient atmosphere with a relative humidity of about 25%; (b) external quantum efficiency (EQE) using NiO films with different annealing temperatures (100–450 °C); (c) J – V curves of the best device based on NiO film annealed at 450 °C, the main photovoltaic parameters are listed in the table; (d) histogram of the device performance obtained from 30 devices.

Table 1 Photovoltaic parameters of the PLD-NiO-based perovskite solar cells as a function of annealing temperature

Buffer layer	Annealing temperature (°C)	V_{oc} (V)	J_{sc} (mA cm ⁻²)	FF (%)	PCE (%)
NiO	As-prepared	0.96	11.39	48.6	5.38
	100	1.02	14.14	53.95	7.91
	200	1.04	14.39	56.82	8.49
	300	1.04	15.9	57.69	9.72
	400	1.02	18.73	62.6	11.9
	450	1.01	19.86	62.78	12.59

due to the bandgap of the $\text{CH}_3\text{NH}_3\text{PbI}_{3-x}\text{Cl}_x$ layer.²¹ With the increase of annealing temperature from 200 °C to 450 °C, the EQE in the whole light absorption region is enhanced constantly. The best-performing device with the NiO film annealed at 450 °C exhibits a remarkable EQE of nearly 88% at around 520 nm and gradually decreases at longer wavelengths indicating a photocurrent loss due to either insufficient absorption of the perovskite layer or optical interference.⁴⁷ The device V_{oc} values with annealed NiO films increase to 1 V as listed in Table 1, which is due to the reduced photocarrier recombination (Fig. 5) and minimized energy loss (Fig. S1, ESI†). The monotonic increase of J_{sc} is partly attributed to the higher optical transmittance of the NiO film after annealing, which is beneficial to improve the utilization efficiency of solar radiation. Another reason is the better crystal quality of the NiO film and the interface between the NiO HTL and the perovskite layer. For inverted planar perovskite solar cells, the morphology and roughness of the NiO film also influence the hole extraction property on the growth of perovskite layers. There is a clear trend of decreasing cell efficiency with increasing surface roughness of the NiO film shown in Fig. 1 and Table 1. As expected, the as-prepared NiO with great roughness exhibiting poor device performance may be due to the decreased charge extraction property owing to the loosely packed and less-ordered microstructure of the NiO film containing a large number of microcracks and voids which have been shown in Fig. 1. When the annealing temperature increases from R.T. to 450 °C, the film surface becomes more smooth and dense and the film crystallization quality becomes better. The corresponding device performance becomes improved. When the photo-carriers transfer across the perovskite film and interfaces to be collected,

the charge recombination usually occurring in the bulk and at the interfaces due to interfacial defects will become smaller,¹³ which can be reflected by the electrochemical impedance spectroscopy (EIS) in Fig. 5. The major FF improvement can be attributed to the improved charge extraction/collection of the NiO film after annealing as a result of enhanced electrical conductivity compared to that without the annealing process. The carrier transport and recombination behaviors in the devices were further investigated by EIS in Fig. 5. Impedance measurements of cells based on the as-prepared NiO film and NiO films annealed at 400 °C and 450 °C were recorded over a frequency range of 1 Hz to 1 MHz with an ac amplitude of 10 mV under 100 mW cm⁻² illumination, in which two distinct frequency regions can be observed. The first arc at a high frequency region is usually related to the carrier transport process at the interface between the perovskite/HTL in the device. While the second arc at lower frequency is usually attributed to the charge recombination within the perovskite film and the interface of the charge transport layer.⁴⁸ The recombination resistances for devices can be extracted by fitting the plots using the circuit shown in Fig. 5(b). As a result, the R_s of the device with the NiO film annealed at 450 °C (R_s : 28.6 Ω) is slightly lower than that of the device with the NiO film annealed at 400 °C (R_s : 47.9 Ω). This indicates that the improved conductivity of the NiO HTL reduces the contact resistance at the perovskite/NiO HTL interface. More importantly, the device with the NiO film annealed at 450 °C also exhibits a lower R_{trans} (19.57 Ω) than that based on the NiO film annealed at 400 °C (R_{trans} : 129.1 Ω). The lower R_{trans} also confirms that improved charge transport of the former as a result of the increased conductivity. However, the device with the as-prepared NiO film exhibits much higher R_{trans} (336.5 Ω) than the others. Therefore, it can be seen that, in the samples annealed at lower temperatures, there remain a lot of grain boundaries and defects between NiO particles which result in the expansion of the first arc.⁴⁹ Furthermore, the device with NiO films annealed at 450 °C shows an increased recombination resistance (R_{rec} : 88.03 Ω) as compared to that of NiO annealed at 400 °C (R_{rec} : 33.02 Ω). It is seen that the device based on NiO annealed at 450 °C displays much lower recombination, seen by higher R_{rec} .⁵⁰ So the impedance analysis clearly demonstrates that the device using the NiO film annealed at 450 °C results in reduced charge recombination

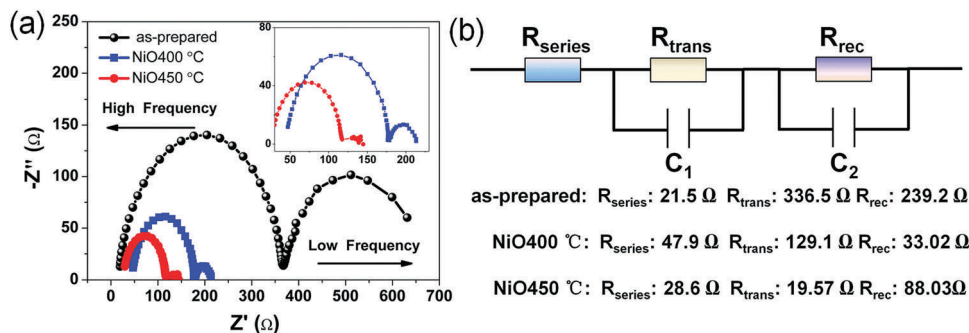


Fig. 5 (a) Nyquist plots of the PVSCs based on the as-prepared NiO film and NiO film annealed at 400 °C and 450 °C, light intensity: 100 mW cm⁻²; (b) equivalent circuit model employed for impedance analysis of the perovskite solar cells.

in the device compared to the devices based on the as-prepared NiO film and the NiO film annealed at 400 °C to further enhance the photovoltaic performance.

Fig. 4(c) show the J - V curves of the best performance cell based on the NiO film annealed at 450 °C and the main photovoltaic parameters are listed in the inset. It shows a decent PCE of 12.59% for the forward scan and 12.58% for the reverse scan, respectively, with very weak hysteresis. Fig. 4(d) displays the statistical histograms of the PCE obtained from 30 devices fabricated with as-prepared and annealed at 450 °C NiO films, respectively. A clearly enhanced cell efficiency is observed for devices with annealed NiO films, and the average PCE of these devices is about 11.33%. The statistical histograms of FF, J_{sc} and V_{oc} are shown in Fig. S9 (ESI[†]). Then these devices are stored in a dry box (RH about 1%) for long term stability measurement. Finally, the photovoltaic performance evolution of one of our best cells after 5 days is presented in Fig. S9 (ESI[†]). The PCE remains 10.1% compared to its original value (12.59%), which indicates a commendable long duration stability with the annealed NiO films. These obtained J - V characteristics are in good agreement with the above surface, crystallinity, and optical changes of the NiO film caused by annealing (Table 1).

2.3 Effect of Li-doping on the NiO film based PSC performance

In order to improve the film conductivity, which can reduce the carrier transport loss in the NiO HTLs, Li^+ ions were incorporated into the p-type NiO films by doping the $\text{NiO}:\text{Li}_x$ target by PLD. XPS was used to analyze the film surface compositions and

chemical states by deconvolving the peak with the Lorentzian–Gaussian function. Fig. 6(a and b) show the XPS spectra of the Ni 2p and O 1s core levels of the NiO and $\text{NiO}:\text{Li}_{0.1}$ films. The Ni 2p peaks in the $\text{NiO}:\text{Li}_{0.1}$ and NiO films can be separated into five distinct peaks that are consistent with previous reports.⁵¹ The Ni 2p_{3/2} peak and its satellite (852.81 eV and 860.16 eV) as well as the Ni 2p_{1/2} peak and its satellite (871.6 and 878.41 eV) are assigned to the Ni^{2+} in NiO. The peak at 854.57 eV is assigned to the Ni^{3+} of Ni_2O_3 .^{52,53} The coexistence of Ni^{2+} and Ni^{3+} states is indicative of the non-stoichiometric nature of the oxygen-rich NiO film. After lithium doping, the XPS of Ni 2p remains almost unchanged, indicating similar Ni components with the pristine NiO sample. However, an obvious change is observed for the O 1s core level after doping. Fig. 6(b) shows the XPS spectra for O 1s in the NiO film, with a peak centered at 528.28 eV, further confirming the octahedral bonding of Ni–O. The peak at 531.25 eV may be ascribed to nickel hydroxides, including defective nickel oxides with hydroxyl groups adsorbed onto the surface.^{54,55} Interestingly, the O 1s peaks for the $\text{NiO}:\text{Li}_{0.1}$ film show a binding energy shift towards the low energy direction compared to that in the NiO film, as shown in Fig. 6(b). Chemical impurities different from NiO can cause XPS peak shift and asymmetry.^{56–58} Also, the relative intensity of the O 1s peak at 528.28 eV obviously increases. These phenomena indicate that Li is successfully involved and causes lattice changes. Two extra weak peaks at 53.76 eV and 55.67 eV shown in Fig. 6(c) further confirm successful Li doping. A peak centered at 53.76 eV pertaining to Li^+ is due to the Li–O bond, indicating that Li atoms enter into the NiO lattice matrix by occupying Ni sites. The peak at

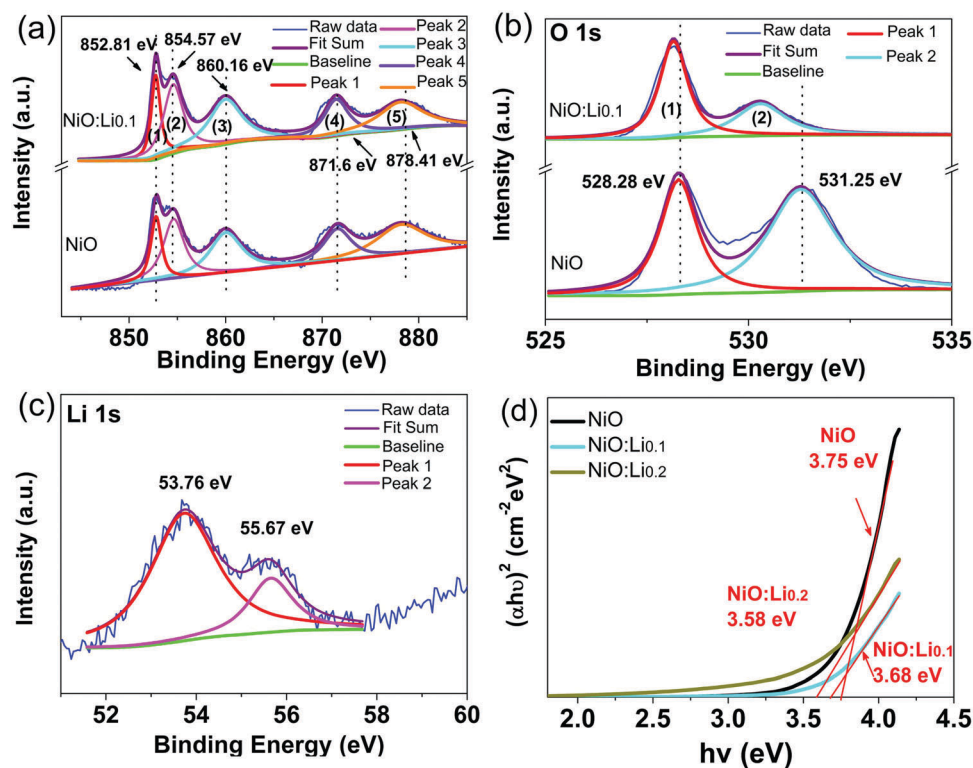


Fig. 6 XPS spectra of NiO and $\text{NiO}:\text{Li}_{0.1}$ thin films annealed at 450 °C by a pulsed laser deposition method for Ni 2p (a); O 1s (b) and Li 1s (c); (d) optical energy band gap of NiO based films as a function of Li doping concentration varied from 0 to 20 mol%.

55.67 eV may be ascribed to the surface defects, such as surface Li ions adsorbed to CO₂ groups in the air.⁵⁹

Moreover, the band gap change of the NiO:Li_x films ($x = 0, 0.1, 0.2$) shown in Fig. 6(d) is also investigated. The optical band gap (E_g) can be calculated by assuming a direct transition between the valence and conduction bands. The absorption coefficient α obeys the following relationship with E_g near the band gap, eqn (4),

$$(\alpha h\nu) \propto A(h\nu - E_g)^n \quad (4)$$

where A is a constant, h is Planck's constant, and ν is the incident photon's frequency. The value of n equals 1/2 or 2 corresponding to the absorption behavior for indirect and direct optical transition, respectively. The optical absorption coefficient (α) can be estimated from two items, consisting of the optical transmittance (T) and the film thickness (d), using eqn (5),

$$\alpha = -(1/d)\ln(T) \quad (5)$$

The corresponding $(\alpha h\nu)^2$ versus $h\nu$ plots for the NiO:Li_x ($x = 0, 0.1, 0.2$) films are shown in Fig. 6(d). The band gap is obtained by extrapolating the linear part of the plot $(\alpha h\nu)^2$ versus $h\nu$ to the energy axis. As a result, the band gap decreases from 3.75 eV to

3.58 eV with the Li doping content increasing from 0 to 0.2. Lower band gap values for Li doped NiO films can be attributed to more stoichiometric defects that cause band tailing.⁶⁰ These phenomena further prove that the Li ions are successfully doped into the NiO films by PLD.

Also, exploring the impact of lithium (Li) doping on the efficacy of inorganic NiO based perovskite solar cells is another important aspect of the device optimization. All other PLD parameters remain unchanged with a constant repetition frequency of 5 Hz and controlling the oxygen partial pressure of 1.33 Pa. The NiO:Li_x films are annealed at 450 °C for 20 min in a rapid annealing furnace. Fig. 7(a) illustrates the J - V curves of the NiO:Li_x/CH₃NH₃PbI_{3-x}Cl_x/PCBM heterojunction cells and the PCE of the NiO:Li_{0.1}-based solar cell is the highest among the three different kinds of devices. The device performance parameters are summarized in Table 2. The doped NiO:Li_{0.1} film improves the photovoltaic performance, giving a V_{oc} of 1.05 V, a J_{sc} of 22.8 mA cm⁻², and a FF of 64.15%, corresponding to a PCE of 15.51%, outperforming the device derived from the pristine NiO film (V_{oc} , J_{sc} , FF, and PCE are 1.01 V, 19.86 mA cm⁻², 62.78%, and 12.59%, respectively). The major

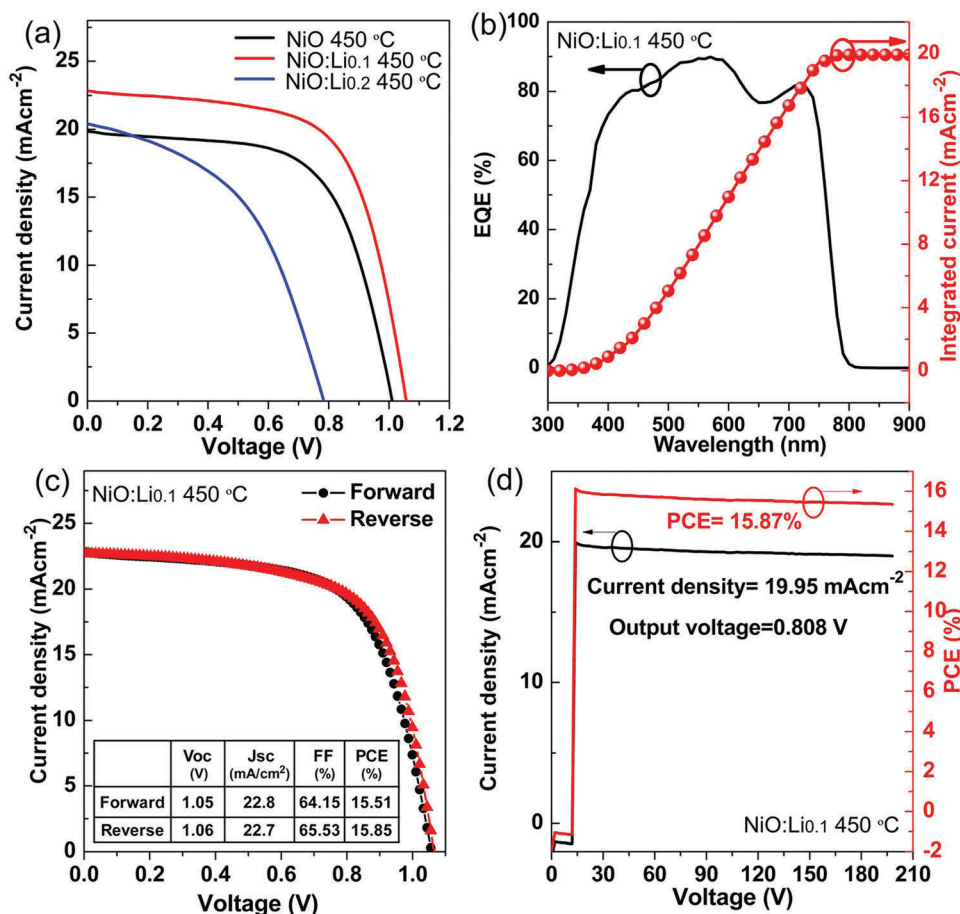


Fig. 7 (a) The photocurrent density–voltage (J - V) curves of perovskite solar cells based on NiO, NiO:Li_{0.1} and NiO:Li_{0.2} films annealed at 450 °C; (b) external quantum efficiency (EQE) using the NiO:Li_{0.1} film annealed at 450 °C (black line). The integrated product of the EQE spectrum with the AM1.5G photon flux is also shown (red line); (c) J - V curves of the best device based on the NiO:Li_{0.1} film annealed at 450 °C; the main photovoltaic parameters are listed in the table. The red line is the reverse scan from the short-circuit conditions, the black line indicates a forward scan starting from the open-circuit conditions; (d) steady-state photocurrent output at the maximum power point (0.808 V).

Table 2 Photovoltaic parameters of the PLD-NiO-based perovskite solar cells as a function of Li doping concentration

Buffer layer	Annealing temperature (°C)	V_{oc} (V)	J_{sc} (mA cm^{-2})	FF (%)	PCE (%)
NiO	450	1.01	19.86	62.78	12.59
NiO:Li _{0.1}	450	1.05	22.8	64.15	15.51
NiO:Li _{0.2}	450	0.78	20.41	47.25	7.56

improvement lies in the increased J_{sc} and FF, which can be attributed to the improved charge extraction/collection of the NiO:Li_{0.1} film as a result of enhanced electrical conductivity compared to the pristine NiO film as shown in Table S7 (ESI[†]). The Li ion has an ionic radius of 0.076 nm, which is slightly larger than that of Ni²⁺ (0.069 nm) and will not cause obvious lattice distortion in a doped crystal. Theoretically, Li has a relative shallower acceptor level in NiO for Ni-poor/O-rich conditions.⁶⁰ The most important defect is the Li substituting Ni (Li_{Ni}), which has $\Delta H < 1$ eV.⁶¹ These properties make Li a potential acceptor dopant. The Li-doped NiO film significantly enhances electrical conductivity, which reduces the carrier transport loss in the HTL. However, for the NiO:Li_{0.2} film-based solar cell, the PCE of the device decreases to 7.56% (Table 2). Too much Li doping introducing more defects deteriorates the crystal quality of the NiO:Li_{0.2} film. Also, with the increase of Li concentration, Li atoms not only occupy the sites of Ni but also the interstitial sites, which upon introducing electrons act as hole killers.¹⁴ The current leakage increases at the interface and in the internal NiO:Li_{0.2} layer by the traps. Accordingly, the series resistance (R_s) of the oxide increases and the shunt resistance (R_{sh}) greatly decreases with respect to the undoped and NiO:Li_{0.1} layers, leading to a not ideal fill factor (FF) with a value of about 0.47. Moreover, J_{sc} and V_{oc} of the NiO:Li_{0.2} film based device are both decreased to 20.41 mA cm^{-2} and 0.78 V. This demonstrates that the doping concentration of Li dramatically affects the recombination dynamics in the device and, therefore, is a significant factor affecting the V_{oc} and FF of PSCs with state-of-the-art perovskite films.⁶² So, higher lithium doping, e.g. NiO:Li_{0.2} does not improve the device performance. The EQE spectrum of the photovoltaic device with the NiO:Li_{0.1} film is also examined and presented in Fig. 7(b). The perovskite solar cell exhibits a broad spectral response from the visible to near-infrared (300 to 800 nm) region and the corresponding EQE value reaches nearly 89% at 550 nm and over 80% from 430 nm to 750 nm. The integrated current density from the EQE spectrum is 20.18 mA cm^{-2} , which is very close to the value from the J - V scanning curves. The J - V characteristics of the device based on the NiO:Li_{0.1} film with both forward ($J_{sc} \rightarrow V_{oc}$) and reverse ($V_{oc} \rightarrow J_{sc}$) scanning curves are shown in Fig. 7(c). The device exhibits negligible hysteresis, which demonstrates that the NiO:Li_{0.1} HTLs could effectively mitigate hysteresis in perovskite solar cells. The main photovoltaic parameters are listed in the inset in Fig. 7(c). In order to examine the device stability and output property, we measured the steady-state photocurrent output at the maximum power point (0.808 V) which has been confirmed in the inset J - V curve (Fig. 7(c)). The steady-state photocurrent represents the actual power

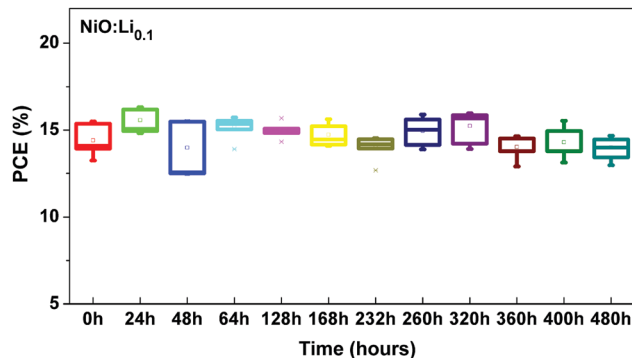


Fig. 8 Power conversion efficiency (PCE) for glass/ITO/NiO:Li_{0.1}/perovskite/PCBM/Ag stored in a glove box for 480 h.

output and should be used to accurately characterize the device efficiency. As shown in Fig. 7(d), the photocurrent increases quickly to the maximum value and the steady-state current fixes at 19.95 mA cm^{-2} for a long duration over 200 s. Also the NiO:Li_{0.1} devices are stored in a glove box (~ 28 °C) for long term stability measurement. Finally, the photovoltaic performance evolution of six of our best cells after 480 h is presented in Fig. 8. The PCE remains at 13.42% compared to its original value (15.51%), which indicates a commendable long duration stability with NiO:Li_{0.1} films. This degradation is generally consistent across 6 devices, indicating good long-term stability. This indicates that the incorporation of Li does not have a bad effect on the stability of the devices compared to the pristine NiO film.

3. Conclusion

In summary, we have performed detailed research about precisely controlling the crystallinity and physical properties of NiO films by post-annealing and lithium doping and their influence on the perovskite solar cell efficiency is also demonstrated. The photovoltaic performance is explored using a P-i-N solar cell with a NiO/CH₃NH₃PbI_{3-x}Cl_x/PCBM/Ag configuration, where the PLD-grown NiO film acts as the HTL. Post-annealing can smooth the NiO film surface and increase its optical transmittance, which are beneficial to improving the PSC efficiency from 5.38% to 12.59% by reducing the photocarrier recombination rate and effective utilization of solar radiation. Successful lithium doped NiO films by PLD increase their electrical conductivity and effectively reduce the carrier transport loss in the HTL. As a result, the device PCE is further improved to 15.51%. So regulating the physical properties of NiO films by post-annealing and doping is essential for developing perovskite solar cells. We expect that the optimized NiO film will be competitive with high-performing MAPbI₃ based N-i-P solar cells and an ideal HTL candidate for perovskite solar cells.

Acknowledgements

This work is supported by NSFC (51472110) and Shandong Provincial Natural Science Foundation (2014ZRB01A47). The research program from the Ministry of Education, China, is

also acknowledged (213021A). BC thanks the Taishan Scholar Professorship tenured at the University of Jinan and the post-graduate innovation project (YCXB15001) from the same University.

References

- 1 Y. H. Cheng, Q. D. Yang, J. Y. Xiao, Q. F. Xue, H. W. Li, Z. Q. Guan, H. L. Yip and S. W. Tsang, *ACS Appl. Mater. Interfaces*, 2015, **7**, 19986–19993.
- 2 H. S. Kim, S. H. Im and N. G. Park, *J. Phys. Chem. C*, 2014, **118**, 5615–5625.
- 3 H. J. Snaith, *J. Phys. Chem. Lett.*, 2013, **4**, 3623–3630.
- 4 M. Z. Liu, M. B. Johnston and H. J. Snaith, *Nature*, 2013, **501**, 395–398.
- 5 J. Even, L. Pedesseau and C. Katan, *J. Phys. Chem. C*, 2014, **118**, 11566–11572.
- 6 Y. Yamada, T. Nakamura, M. Endo, A. Wakamiya and Y. Kanemitsu, *IEEE J. Photovolt.*, 2015, **5**, 401–405.
- 7 Q. Lin, A. Armin, R. C. R. Nagiri, P. Burn and P. Meredith, *Nat. Photonics*, 2015, **9**, 106–112.
- 8 Q. Chen, H. P. Zhou, Z. R. Hong, S. Luo, H. S. Duan, H. H. Wang, Y. S. Liu, G. Li and Y. Yang, *J. Am. Chem. Soc.*, 2014, **136**, 622–625.
- 9 J. H. Im, I. H. Jang, N. Pellet, M. Graetzel and N. G. Park, *Nat. Nanotechnol.*, 2014, **9**, 927–932.
- 10 W. Nie, H. Tsai, R. Asadpour, J. C. Blancon, A. J. Neukirch, G. Gupta, J. J. Crochet, M. Chhowalla, S. Tretiak, M. A. Alam, H. L. Wang and A. D. Mohite, *Science*, 2015, **347**, 522–525.
- 11 J. H. Heo, H. J. Han, D. Kim, T. K. Ahn and S. H. Im, *Energy Environ. Sci.*, 2015, **8**, 1602–1608.
- 12 E. J. Juarez-Perez, M. Wüßler, F. Fabregat-Santiago, K. Lakus-Wollny, E. Mankel, T. Mayer, W. Jaegermann and I. Mora-Sero, *J. Phys. Chem. Lett.*, 2014, **5**, 680–685.
- 13 J. J. Shi, X. Xu, D. M. Li and Q. B. Meng, *Small*, 2015, **11**, 2472–2486.
- 14 J. H. Zhang, G. F. Cai, D. Zhou, H. Tang, X. L. Wang, C. D. Guab and J. P. Tu, *J. Mater. Chem. C*, 2014, **2**, 7013–7021.
- 15 M. H. Kumar, N. Yantara, S. Dharani, M. Graetzel, S. Mhaisalkar, P. P. Boix and N. Mathews, *Chem. Commun.*, 2013, **49**, 11089–11091.
- 16 M. D. Irwin, B. Buchholz, A. W. Hains, R. P. H. Chang and T. J. Marks, *Proc. Natl. Acad. Sci. U. S. A.*, 2008, **5**, 2783–2787.
- 17 M. Jorgensen, K. Norrman and F. C. Krebs, *Sol. Energy Mater. Sol. Cells*, 2008, **92**, 686–714.
- 18 K. Norrman, M. V. Madsen, S. A. Gevorgyan and F. C. Krebs, *J. Am. Chem. Soc.*, 2010, **132**, 16883–16892.
- 19 R. Betancur, M. Maymo, X. Elias, L. T. Vuong and J. Martorell, *Sol. Energy Mater. Sol. Cells*, 2011, **95**, 735–739.
- 20 K. C. Wang, P. S. Shen, M. H. Li, S. Chen, M. W. Lin, P. Chen and T. F. Guo, *ACS Appl. Mater. Interfaces*, 2014, **6**, 11851–11858.
- 21 J. Y. Jeng, K. C. Chen, T. Y. Chiang, P. Y. Lin, T. D. Tsai, Y. C. Chang, T. F. Guo, P. Chen, T. C. Wen and Y. J. Hsu, *Adv. Mater.*, 2014, **26**, 107.
- 22 K. C. Wang, J. Y. Jeng, P. S. Shen, Y. C. Chang, E. W. Diau, C. H. Tsai, T. Y. Chao, H. C. Hsu, P. Y. Lin, P. Chen, T. F. Guo and T. C. Wen, *Sci. Rep.*, 2014, **4**, 4756.
- 23 C. C. Wu and W. C. Shih, *Chem. Commun.*, 2017, **53**, 1634–1637.
- 24 L. Zhao, G. Su, W. Liu, L. Cao, J. Wang, Z. Dong and M. Song, *Appl. Surf. Sci.*, 2011, **257**, 3974.
- 25 D. P. Joseph, M. Saravanan, B. Muthuraaman, P. Renugambal, S. Sambasivam, S. P. Raja, P. Maruthamuthu and C. Venkateswaran, *Nanotechnology*, 2008, **19**, 485707.
- 26 J. H. Park, J. W. Seo, S. M. Park, S. S. Shin, Y. C. Kim, N. J. Jeon, H. W. Shin, T. K. Ahn, J. H. Noh, S. C. Yoon, C. S. Hwang and S. Il Seok, *Adv. Mater.*, 2015, **27**, 4013–4019.
- 27 J. Burschka, N. Pellet, S. J. Moon, R. H. Baker, P. Gao, M. K. Nazeeruddin and M. Grätzel, *Nature*, 2013, **499**, 316–319.
- 28 K. Mahmood, B. S. Swain and H. S. Jung, *Nanoscale*, 2014, **6**, 9127–9138.
- 29 X. G. Yu, T. J. Marks and A. Facchetti, *Nat. Mater.*, 2016, **15**, 383–396.
- 30 J. Cui, F. P. Meng, H. Zhang, K. Cao, H. L. Yuan, Y. B. Cheng, F. Huang and M. K. Wang, *ACS Appl. Mater. Interfaces*, 2014, **6**, 22862–22870.
- 31 W. L. Jang, Y. M. Lu, W. S. Hwang, T. L. Hsiung and H. P. Wang, *Appl. Phys. Lett.*, 2009, **94**, 062103.
- 32 S. Mrowec and Z. Grzesik, *J. Phys. Chem. Solids*, 2004, **65**, 1651–1657.
- 33 D. S. Ginger and N. C. Greenham, *Phys. Rev. B: Condens. Matter Mater. Phys.*, 1999, **59**, 10622–10629.
- 34 J. Burschka, N. Pellet, S. J. Moon, B. R. Humphry, P. Gao, M. K. Nazeeruddin and M. Gratzel, *Nature*, 2013, **499**, 316–319.
- 35 Y. J. Qi, H. Y. Qi, J. H. Li and C. J. Lu, *J. Cryst. Growth*, 2008, **310**, 4221–4225.
- 36 P. Qin, N. Tetreault, M. I. Dar, P. Gao, K. L. McCall, S. R. Rutter and S. D. Ogier, *Adv. Energy Mater.*, 2014, **5**, 980–984.
- 37 D. A. Guzmán-Embús, M. F. Vargas-Charry and C. Vargas-Hernández, *J. Am. Chem. Soc.*, 2015, **98**, 1498–1505.
- 38 T. Y. Zhang, N. J. Guo, G. Li, X. F. Qian and Y. X. Zhao, *Nano Energy*, 2016, **26**, 50–56.
- 39 C. Quarti, G. Grancini, E. Mosconi, P. Bruno, J. M. Ball, M. M. Lee, H. J. Snaith, A. Petrozza and F. D. Angelis, *J. Phys. Chem. Lett.*, 2014, **5**, 279–284.
- 40 F. T. Thema, E. Manikandan, A. G. Fakim and M. Maaza, *J. Alloys Compd.*, 2016, **657**, 655–661.
- 41 S. Nakashima, *Solid State Commun.*, 1975, **16**, 1059–1062.
- 42 V. Capozzi, A. Fontana, M. Fontana, G. Mariotto, M. Montagna and G. Viliani, *Il NuovoCimento B*, 1977, **39**, 556–568.
- 43 R. Zallen and M. L. Slade, *Solid State Commun.*, 1975, **17**, 1561–1566.
- 44 R. Gottesman, L. Gouda, B. S. Kalanoor, E. Haltzi, S. Tirosh, E. R. Hodesh, Y. Tischler and A. Zaban, *J. Phys. Chem. Lett.*, 2015, **6**, 2332–2338.
- 45 Y. Z. Ma, L. L. Zheng, Y. H. Chung, S. S. Chu, L. X. Xiao, Z. J. Chen, S. F. Wang, B. Qu, Q. H. Gong, Z. X. Wu and X. Hou, *Chem. Commun.*, 2014, **50**, 12458–12461.
- 46 L. Fan, Y. Ding, J. S. Luo, B. Shi, X. Yao, C. C. Wei, D. Zhang, G. C. Wang, Y. Sheng, Y. F. Chen, A. Hagfeldt, Y. Zhao and X. D. Zhang, *J. Mater. Chem. A*, 2017, **5**, 7423–7432.

- 47 H. P. Zhou, Q. Chen, G. Li, S. Luo, T. B. Song, H. Duan, Z. R. Hong, J. B. You, Y. S. Liu and Y. Yang, *Science*, 2014, **345**, 542–546.
- 48 J. W. Jung, C. C. Chuen and A. K. Y. Jen, *Adv. Mater.*, 2015, **27**, 7874–7880.
- 49 T. Hoshikawa, M. Yamada, R. Kikuchi and K. Eguchi, *J. Electrochem. Soc.*, 2005, **152**, 68–73.
- 50 X. T. Yin, P. Chen, M. D. Que, Y. L. Xing, W. X. Que, C. M. Niu and J. Y. Shao, *ACS Nano*, 2016, **10**, 3630–3636.
- 51 M. S. Sawanta, K. Hyungjin, E. S. Sang and K. H. Chang, *Nanoscale*, 2016, **8**, 19189–19194.
- 52 X. T. Yin, P. Chen, M. D. Que, Y. L. Xing, W. X. Que, C. M. Niu and J. Y. Shao, *ACS Nano*, 2016, **10**, 3630–3636.
- 53 F. Jiang, W. C. H. Choy, X. C. Li, D. Zhang and J. Q. Cheng, *Adv. Mater.*, 2015, **27**, 2930–2937.
- 54 J. R. Manders, S. W. Tsang, M. J. Hartel, T. H. Lai, S. Chen, C. M. Amb, J. R. Reynolds and F. So, *Adv. Funct. Mater.*, 2013, **23**, 2993–3001.
- 55 Y. S. Wang, W. Y. Rho, H. Y. Yang, T. Mahmoudi, S. H. Seo, D. H. Lee and Y. B. Hahn, *Nano Energy*, 2016, **27**, 535–544.
- 56 T. Dutta, P. Gupta, A. Gupta and J. Narayan, *J. Appl. Phys.*, 2010, **108**, 083715.
- 57 M. N. Islam, T. B. Ghosh, K. L. Chopra and H. N. Achary, *Thin Solid Films*, 1996, **280**, 20–25.
- 58 X. L. Hu, H. B. Gong, H. Y. Xu, H. M. Wei, B. Q. Cao, G. Q. Liu, H. B. Zeng and W. P. Cai, *J. Am. Chem. Soc.*, 2011, **94**, 4305–4309.
- 59 W. Chen, Y. Z. Wu, Y. F. Yue, J. Liu, W. J. Zhang, X. D. Yang, H. Chen, E. Bi, I. Ashraful, M. Grätzel and L. Y. Han, *Science*, 2015, **350**, 944–948.
- 60 T. Dutta, P. Gupta, A. Gupta and J. Narayan, *J. Appl. Phys.*, 2010, **108**, 083715.
- 61 J. Osorio-Guillén, S. Lany, A. Zunger, M. Caldas and N. Studart, *AIP Conference Proceedings*, 2010, vol. 1199, pp. 128–129.
- 62 J. Correa-Baena, W. Tress, K. Domanski, E. H. Anaraki, S. Turren-Cruz, B. Roose, P. P. Boix, M. Grätzel, M. Saliba, A. Abate and A. Hagfeldt, *Energy Environ. Sci.*, 2017, **10**, 1207–1212.